Quantitative Analysis of Pleural Line and B-Lines in Lung Ultrasound Images for Severity Assessment of COVID-19 Pneumonia

Yuanyuan Wang, *Student Member, IEEE*, Yao Zhang, Qiong He, *Member, IEEE*, Hongen Liao, *Senior Member, IEEE*, and Jianwen Luo, *Senior Member, IEEE*

***Abstract*— Specific patterns of lung ultrasound (LUS) images are used to assess the severity of coronavirus disease 2019 (COVID-19) pneumonia, while such assessment is mainly based on clinicians' qualitative and subjective observations. In this study, we quantitatively analyze the LUS images to assess the severity of COVID-19 pneumonia by characterizing the patterns related to the pleural line (PL) and B-lines (BLs). Twenty-seven patients with COVID-19 pneumonia, including 13 moderate cases, seven severe cases, and seven critical cases, are enrolled. Features related to the PL, including the thickness (TPL) and roughness of the PL (RPL), and the mean (MPLI) and standard deviation (SDPLI) of the PL intensities are extracted from the LUS images. Features related to the BLs, including the number (NBL), accumulated width (AWBL), attenuation coefficient (ACBL), and accumulated intensity (AIBL) of BLs, are also extracted. The correlations of these features with the disease severity are evaluated. The performances of the binary severe/non-severe classification are assessed for each feature and support vector machine (SVM) classifiers with various combinations of features as input. Several features, including the RPL, NBL, AWBL, and AIBL, show significant correlations with disease severity (all $p < 0.05$). The classification performance is optimal using the SVM classifier using all the features as input (area under the receiver operating characteristic (ROC) curve = 0.96, sensitivity = 0.93, and specificity = 1). These findings demonstrate that the proposed method may be a promising tool for automatic grading diagnosis and follow-up of patients with COVID-19 pneumonia.**

Manuscript received July 14, 2021; accepted August 21, 2021. Date of publication August 24, 2021; date of current version December 30, 2021. This work was supported in part by the Tsinghua University Spring Breeze Fund under Grant 2021Z99CFY025; in part by the National Natural Science Foundation of China under Grant 61871251, Grant 61801261, and Grant 62027901; in part by Sichuan Science and Technology Program under Grant 2019YFSY0048; in part by Tsinghua-Peking Joint Center for Life Sciences; and in part by the Young Elite Scientists Sponsorship by China Association for Science and Technology. *(Yuanyuan Wang and Yao Zhang contributed equally to this work.) (Corresponding authors: Yao Zhang; Jianwen Luo.)*

This work involved human subjects or animals in its research. Approval of all ethical and experimental procedures and protocols was granted by the Local Ethics Committee of Beijing Ditan Hospital.

Yuanyuan Wang, Qiong He, Hongen Liao, and Jianwen Luo are with the Department of Biomedical Engineering, School of Medicine, Tsinghua University, Beijing 100084, China (e-mail: luo_jianwen@tsinghua.edu.cn).

Yao Zhang is with the Department of Ultrasound, Beijing Ditan Hospital, Capital Medical University, Beijing 100015, China (e-mail: zgzsy007@163.com).

Digital Object Identifier 10.1109/TUFFC.2021.3107598

***Index Terms*— B-line (BL), coronavirus disease 2019 (COVID-19) pneumonia, pleural line (PL), quantitative analysis, severity assessment.**

I. Introduction

SINCE the outbreak of the coronavirus disease 2019 (COVID-19) caused by severe acute respiratory syndrome coronavirus 2 (SARS-CoV-2) in December 2019, it has spread rapidly around the world, and the number of infections and deaths has increased dramatically [1]. COVID-19 pneumonia can progress into a very severe condition rapidly, and thus fast and accurate evaluation of the morbid lesions and lung conditions is significant for timely and proper treatment of patients. Reverse transcription polymerase chain reaction (PT-PCR) is currently used as the gold standard for confirming the infection of SARS-CoV-2. However, it suffers from long testing time and low sensitivity, and it is not applicable to assess the disease's severity [2], [3]. Chest computed tomography (CT) is considered to be a reliable imaging modality in clinic for the diagnosis of COVID-19 pneumonia, but it is highly irradiative and expensive and has the risk of cross infection, and thus it is not suitable as a bedside tool for follow-up of critically ill patients [4]–[8].

As an alternative, lung ultrasound (LUS) imaging (i.e., lung ultrasonography) has the advantages of being noninvasive, ionizing radiation-free, real-time, cost-effective, and portable and can serve as a helpful and reliable bedside tool to evaluate and monitor the lung conditions of critically ill patients in the intensive care unit (ICU) [9]–[15]. LUS imaging reveals the pathological conditions of the lung based on different patterns of imaging artifacts in the B-mode images. Under the normal condition of the lung, the soft-tissue/air interface, i.e., the pleural line (PL), causes multiple reflections of ultrasound pulses between the transducer and the PL, which behave as multiple equidistant artifacts parallel to the PL. These artifacts are known as A-lines [16]. Under the ill condition of the lung, hyper-echoic vertical lines which originate from PL and stretch to the bottom of the imaging field of view can be observed and are known as B-lines (BLs). Their distribution characteristics are found to be correlated with the pathological conditions of the lung in several studies [17]–[19].

In the diagnosis and treatment of COVID-19 pneumonia, specific LUS patterns are used to assess the severity of the lung

conditions, which include the thickening of the PL, the confluence of BLs, and the presence of lung consolidations [8], [10], [20]–[31]. However, such assessment is based on qualitative and subjective observations made by the clinicians. Some semiquantitative methods, i.e., the scoring systems based on visual observations of the line artifacts, and quantitative methods based on automatic detection of PL and BLs have been proposed for diagnosis, evaluation, and follow-up of patients with COVID-19 pneumonia. Nevertheless, these approaches mainly focus on the features related to the characteristics of PL and BLs separately [20], [32], [33]. The characteristics associated with PL and BLs are not combined to evaluate the lung conditions. Besides, automatic diagnostic systems based on deep learning have shown promises for fast and accurate diagnosis of COVID-19 pneumonia using the quantitative indices extracted from BLs, the frame-level or video-level ultrasound images, or the combination of the images and clinical information as input [34]–[37], but these methods require a large number of annotated samples from patients with COVID-19 pneumonia, which are difficult to obtain.

Based on the aforementioned imaging patterns related to disease severity, we propose a novel method to assess the severity of COVID-19 pneumonia in this study. Specifically, we extract a series of quantitative features related to PL and BLs by analyzing the LUS images from patients diagnosed with various degrees of COVID-19 pneumonia. The disease severity of these patients is clinically classified into three categories, namely, moderate cases, severe cases, and critical cases. To evaluate the performance of the proposed features in evaluating the disease severity, we compare the features corresponding to different cases and study the correlations between the features and the disease severity. Fast and reliable identification of severe patients, including severe cases and critical cases, arises more concerns of the clinicians in terms of timely treatment and reduction in the overall mortality of COVID-19 pneumonia. To this end, we analyze the performance of each feature in binary classification of severe and non-severe patients and further use a support vector machine (SVM) classifier to improve the classification performance.

II. Methods

A. Study Protocol

This study was approved by the local ethics committee of Beijing Ditan Hospital, and the need for written informed consent was waived due to the retrospective nature of the study. Twenty-seven patients confirmed as affected by COVID-19 virus using RT-PCR test, who were hospitalized from March 2 to March 30, 2020, were included in this study. According to Chinese diagnosis and treatment protocol for COVID-19 pneumonia (seventh edition) [38], the patients can be categorized into four cases, namely, mild cases, moderate cases, severe cases, and critical cases. Mild cases have only mild clinical symptoms and have no chest imaging manifestations of pneumonia, and thus were not enrolled in this study. Moderate cases have symptoms of fever and respiratory as well as imaging findings of pneumonia. Severe cases have symptoms of respiratory distress or arterial partial pressure of oxygen/fraction of inspired oxygen lower than 300 mmHg, or oxygen saturation less than 93% at rest. Critical cases have symptoms of respiratory failure, or shock, or other organ failure requiring ICU care. According to these classification criteria, the enrolled patients ($n = 27$) were classified into three cases, namely, moderate cases ($n = 13$), severe cases ($n = 7$), and critical cases ($n = 7$). In the investigation of binary classification (severe/non-severe), severe cases and critical cases were defined as severe patients, and moderate cases were defined as non-severe patients. The characteristics we collected for each patient included gender, age, clinical symptoms, concomitant diseases, and laboratory tests. Each patient underwent an LUS examination performed by an experienced clinician using a Hi Vision Preirus system (Hitachi Healthcare, Tokyo, Japan) equipped with an EUP-C715 convex probe (5–1 MHz). The dynamic range was kept constant at 65 dB for all the patients. The imaging parameters, including the imaging depth, overall gain, time gain compensation (TGC), and focal depth, were slightly tuned during the examination to obtain the best possible imaging field of view and image quality for different patients. During the examination, each patient was in the supine position, and six regions of each half-chest were determined, including the anterior, lateral, and posterior parts of the upper and lower halves [39]–[41]. All the intercostal spaces of these regions provide acoustic windows for lung assessment and were carefully examined. For each region, the image with the most serious image pattern in one or several intercostal spaces was recorded and considered as a representative image. Therefore, 12 ultrasound images were acquired in a complete lung ultrasound examination for each patient.

B. Quantitative Analysis of LUS Images

1) Image Preparation: Imaging patterns related to the severity of COVID-19 pneumonia include thickening and disruption of PL, confluence of BLs (including white lung), and lung consolidations. In this study, we focus on analyzing the characteristics of PL and BLs. Before analysis, the LUS images were first normalized in terms of pixel intensity and size by dividing by their respective maximum pixel value and interpolating to the same physical size (i.e., 0.256×0.256 mm^2) to minimize the effects of varying overall gains and imaging depths, respectively.

2) Analysis of the PL: The schematic overview of the PL analysis procedure is presented in Fig. 1. The PL was semiautomatically segmented from each normalized image by manually selecting a region of interest (ROI) around the PL [indicated by red lines in Fig. 1(b)]. The center of the PL was subsequently identified automatically by finding the location with peak intensity within the ROI for each column [indicated by blue points in Fig. 1(c)]. Thickening and disruption of the PL can influence the thickness, intensity, intensity variation, and morphological continuity of the PL. Therefore, these features were extracted from LUS images and defined as follows, respectively.

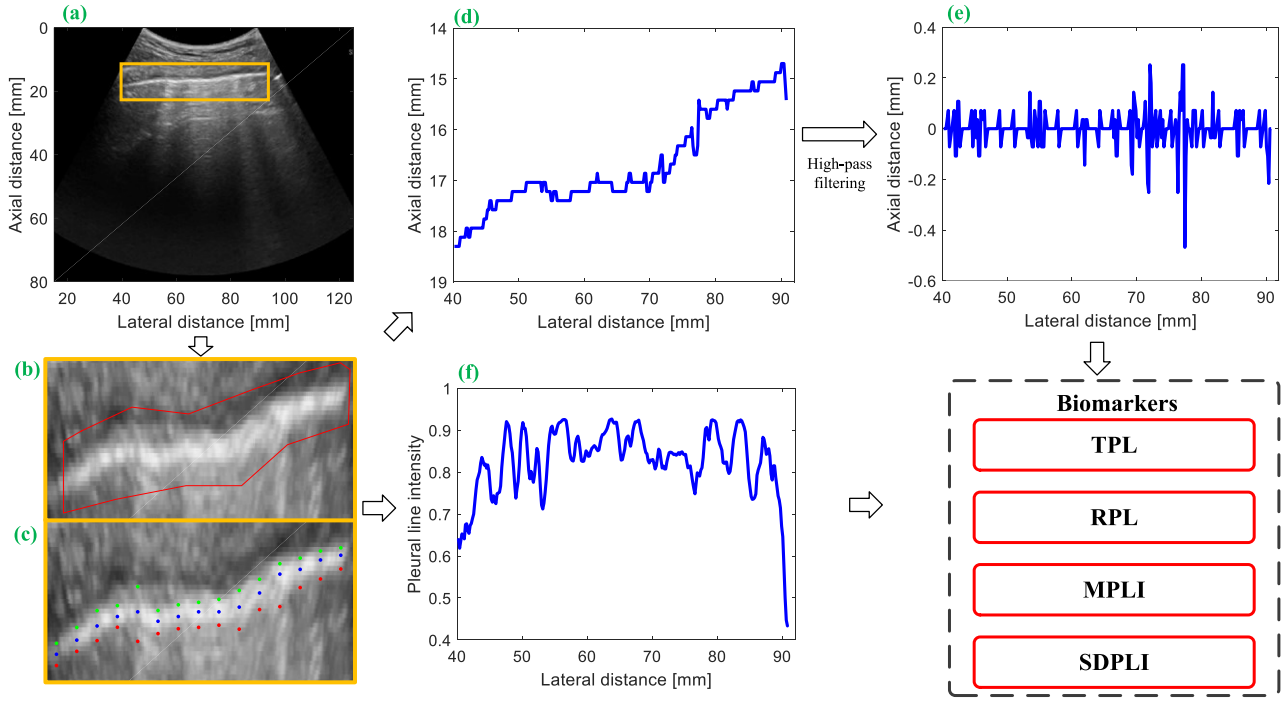

Fig. 1. Schematic of PL analysis procedure. (a) Normalized LUS image. (b) Manual selection of PL. (c) Automatic detection of the anterior location, the center, and the posterior location of PL. (d) Depth profile corresponding to the center of PL. (e) High-pass filtered signal of (d). (f) Intensity profile corresponding to the center of PL. TPL = thickness of PL, RPL = roughness of PL, MPLI = mean of PL intensities, and SDPLI = SD of PL intensities.

a) Thickness of the PL (TPL): For each column, an axial profile within the selected ROI is extracted from the B-mode image, and the intersections of the axial profile and the line with 75% of the maximum intensity are detected. The intersections upper and lower than the PL are defined as the anterior and posterior locations of the PL, which are indicated by green and red points in Fig. 1(c), respectively. TPL is obtained by calculating the average distance between the anterior and posterior locations of the PL as follows:

$$\mathrm{TPL} = \sum_{k=k_s}^{k_e} \frac{d_p(k) - d_a(k)}{(k_e - k_s + 1)} \tag{1}$$

where k is the index of column in the image, k_s and k_e represent the starting and ending columns of the PL, respectively, and d_p and d_a denote the depths of the posterior and anterior locations of the PL, respectively.

b) Roughness of the PL (RPL): The depth profile d_c is obtained after determining the center of the PL, as shown in Fig. 1(d). The contour of the PL is eliminated by high-pass filtering the depth profile with a first-order Butterworth filter, as shown in Fig. 1(e), and RPL is calculated from the filtered signal, d_{ch}, as follows:

$$\mathrm{RPL} = \sqrt{\frac{1}{(k_e - k_s + 1)} \sum_{k=k_s}^{k_e} \left(d_{\mathrm{ch}}(k) - \overline{d_{\mathrm{ch}}}\right)^2} \tag{2}$$

where $\overline{d_{\mathrm{ch}}}$ is the mean amplitude of the filtered signal. Large variation in the filtered signal is considered as a potential indicator of the morphological irregularity of the PL.

c) Mean of the PL Intensities (MPLI): The PL appears continuous and has high intensity in a healthy lung. In contrast, in the pathological lung, the presence of vertical artifacts and consolidations may impact the intensity and continuity of the PL. Thus, the mean and standard deviation (SD) of the PL peak intensities, as shown in Fig. 1(f), are computed as potential indicators of disease severity as follows:

$$\mathrm{MPLI} = \sum_{k=k_s}^{k_e} \frac{I(d_c(k), k)}{(k_e - k_s + 1)} \tag{3}$$

where I is the normalized image data and $d_c(k)$ is the depth of the central PL for the kth column.

d) SD of the PL Intensities (SDPLI):

$$\mathrm{SDPLI} = \sqrt{\frac{1}{(k_e - k_s + 1)} \sum_{k=k_s}^{k_e} \left(I(d_c(k), k) - \mathrm{MPLI}\right)^2} \tag{4}$$

3) Analysis of BLs: The schematic representation of the BL analysis procedure is illustrated in Fig. 2. Before quantitative analysis, the LUS image acquired by a convex probe [Fig. 2(a)] is mapped into a linear grid converted from a polar to a Cartesian coordinate system. Because the distribution pattern and acoustic reflection characteristics of BLs are potential indicators of the pathological conditions of the lung, in this study, several features are extracted from the LUS images to quantify these characteristics.

a) Number of BL (NBL): NBL is counted based on the transformed images, as shown in Fig. 2(b). The counting protocol is the same as that recommended in [42]. Specifically, for each scanned region, the NBL is 1 if a separate BL is detected. If a white lung pattern is observed, the NBL is regarded as ten.

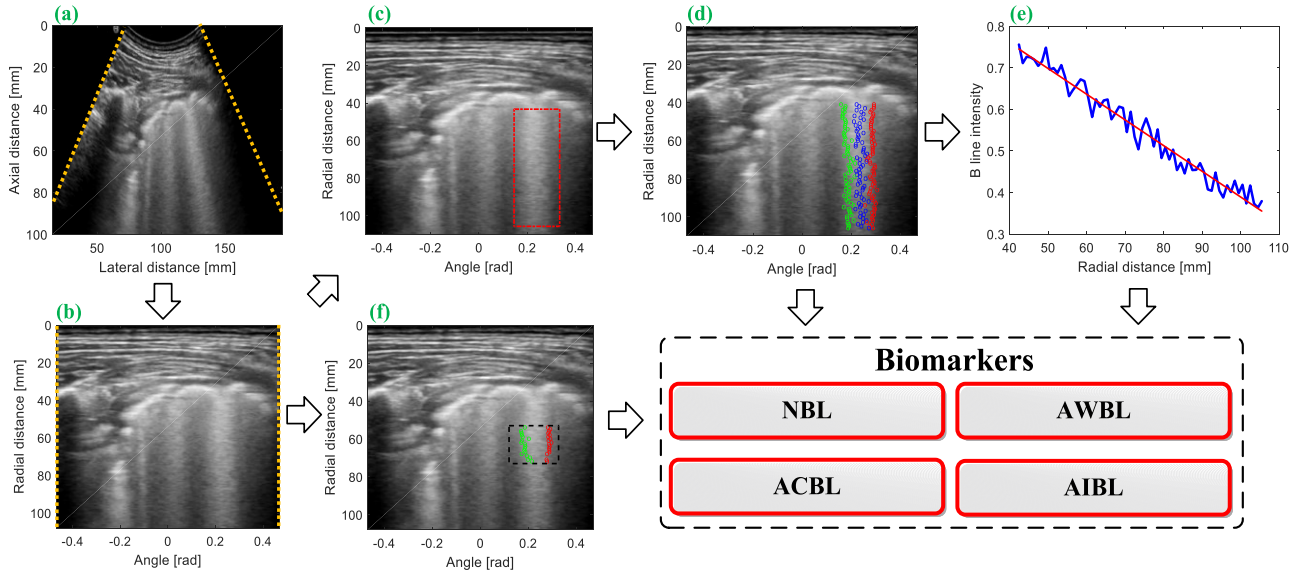

Fig. 2. Schematic of BL analysis procedure. (a) Normalized LUS image. (b) Transformed image obtained by mapping (a) into a linear grid converted from a polar to a Cartesian system. (c) Manual selection of the BL region. (d) Automatic detection of the left boundary, the center, and right boundary of BL. (e) Linear regression between peak intensities on BL and the corresponding axial positions provides the estimation of attenuation coefficient. (f) Intensities of the pixels inside the selected rectangle and between the left and right boundaries of BL are used to calculate BL intensity. NBL = number of BLs, AWBL = accumulated width of BLs, ACBL = attenuation coefficient of BLs, and AIBL = accumulated intensity of BLs.

For confluent BLs that do not cover the entire space, the NBL is calculated as the percentage of the space filled with the confluence BLs multiplied by ten. NBL for each region is calculated by summing all the NBLs in space. The final NBL for each patient is obtained as the summations of NBLs from all the 12 scanned regions (ranging from 0 to 120).

b) Accumulated Width of B-Lines (AWBL): On the transformed image, a rectangle ROI [indicated by red lines in Fig. 2(c)] is manually selected around each BL for the calculation of BL width and attenuation coefficient. For each row inside the ROI, a lateral profile is extracted, and the location with the maximum intensity is defined as the center of BL [indicated by blue points in Fig. 2(d)]. The intersections of the lateral profile and the line with 75% of the maximum intensity are detected and the ones located on the left and right sides of BL center are identified as the left and right boundaries of BL, which are indicated by green and red points in Fig. 2(d), respectively. For each BL, the distances between the boundaries at different rows inside the ROI are averaged and normalized by the length of the PL as the normalized BL width. For each LUS image, the AWBL is calculated by summing the normalized widths of different BLs as follows:

$$\text{AWBL} = \sum_{n=1}^{N} \sum_{r=r_s}^{r_e} \frac{k_r(n,r) - k_l(n,r)}{(k_r - k_l + 1)} \tag{5}$$

where n and N are the index and NBL in the LUS image, respectively. r is the index of the row in the image. r_s and r_e are the starting and ending rows of the selected ROI, respectively. k_r and k_l are the column indices of the right and left boundaries of each BL, respectively.

c) Attenuation Coefficient of B-Lines (ACBL): The center positions of each BL [indicated by blue points in Fig. 2(d)] can be identified from the transformed image by finding the locations with peak intensities for different axial positions. Afterward, linear regression is performed between the peak intensities and the corresponding axial positions, and the attenuation coefficient of each BL is calculated as the slope of the fitting line [Fig. 2(e)]. For each LUS image, the ultimate ACBL (in dB/cm) is calculated as the absolute value of the average attenuation coefficient (in 1 cm) of different BLs, multiplied by the dynamic range, i.e., 65 dB.

d) Accumulated Intensity of B-Lines (AIBL): For each BL, a rectangle ROI with a depth of 2 cm, starting from 1.5 cm blow the PL, is selected for the calculation of BLs' intensity [indicated by dashed black lines in Fig. 2(f)]. The intensity of each BL is calculated by summing the intensities of pixels inside the ROI and between the left [indicated by green points in Fig. 2(f)] and right boundaries [indicated by red points in Fig. 2(f)] of the BL. The ultimate intensity of BLs for each LUS image is obtained by accumulating the intensities of different BLs.

4) Statistical Analysis: For each patient, the PL-related features and ACBL calculated from different images are averaged by the number of analyzed images for statistics analysis. In addition, the number, AWBL, and AIBL corresponding to different images are summed for statistics analysis. To evaluate the performance of these features in grading the severity of COVID-19 pneumonia, one-way analysis of variance (ANOVA) and least significance difference (LSD) tests are used to compare the features among moderate cases, severe cases, and critical cases. The correlations between features and disease severity are determined by calculating Spearman's correlation coefficient (r). A p value less than 0.05 is indicative of statistically significant difference. Performance of each feature in binary classification is assessed by obtaining the receiver operating characteristics (ROC) curve and computing the area under the ROC curve (AUC). Sensitivity (SEN) and

TABLE I
CLINICAL CHARACTERISTICS OF PATIENTS WITH COVID-19 PNEUMONIA

Clinical characteristics	All patients ($n = 27$)	Disease type		
		Moderate cases ($n = 13$)	Severe cases ($n = 7$)	Critical cases ($n = 7$)
Sex (% male)	51.85	53.85	57.14	42.86
Age (years, mean ± SD)	59.89 ± 18.06	54.15 ± 18.17	55.14 ± 17.02	75.29 ± 9.45
Fever (%)	77.78	33.33	100	71.43
Cough (%)	48.15	14.81	57.14	71.43
Shortness of breath (%)	37.04	3.70	42.86	85.71
Concomitant diseases (%)	59.26	22.22	57.14	85.71
Leucocytes decreased (%)	14.81	0	0	57.14
C-reactive protein increased (%)	37.04	0	57.14	85.71

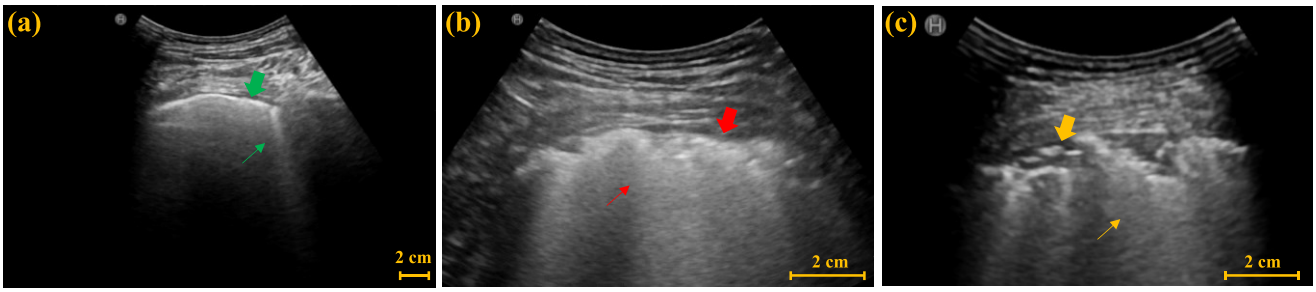

Fig. 3. Examples of LUS images from (a) moderate case, (b) severe case, and (c) critical case. Green thick arrow and thin arrow in (a) indicate a normal PL and a single BL, respectively. Red thick arrow and thin arrow in (b) indicate the thickened and irregular PL and the confluent BLs, respectively. Yellow thick arrow and thin arrow in (c) indicate the interrupted PL and the confluent BLs, respectively.

specificity (SPC) corresponding to the optimal cut-off value on the ROC curve, which is determined by finding the cutoff value with the maximum Youden's index (YI = SEN + SPC − 1), are also presented.

C. SVM Classifiers

Three SVM classifiers are implemented based on the leave-one-out cross-validation method to improve the discrimination performance, using four features related to the PL, four features related to BLs, and their combination as the input of SVMs, respectively. The leave-one-out cross-validation uses a single patient as the validation set and the other patients as the training set. This procedure is repeated until each patient is used once as the validation set. A Gaussian kernel function is used to map the distance of each sample to the decision boundary of each SVM classifier. The classification efficiency of various combinations of the features is assessed by estimating the AUC under the ROC curve. The SEN and SPC corresponding to the optimal cut-off value on the ROC curve are determined as well.

III. RESULTS

A. Clinical and LUS Characteristics

Table I shows the clinical characteristics of patients with COVID-19 pneumonia. Compared with moderate cases, severe cases and critical cases have larger proportions of clinical symptoms such as fever, cough, shortness of breath, larger proportion of concomitant diseases, and larger proportions of hematological manifestations such as decrease in leukocytes and increase in C-reactive protein. The LUS characteristics are illustrated in Fig. 3. As shown, thickening, irregularity, and interruption of PL, and the confluence of BLs are observed with the aggravation of the disease.

B. Severity Assessment of COVID-19 Pneumonia

Figs. 4 and 5 present the comparison results of the features related to PL and BLs among patients of different cases and the

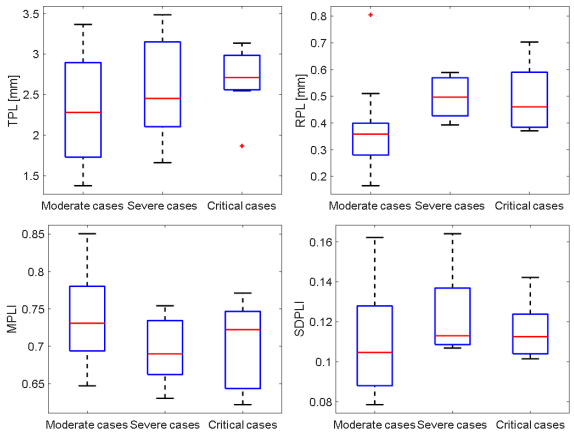

Fig. 4. Comparisons of the PL-related features among moderate cases ($n = 13$), severe cases ($n = 7$), and critical cases ($n = 7$) patients. TPL = thickness of PL, RPL = roughness of PL, MPLI = mean of PL intensities, and SDPLI = SD of PL intensities.

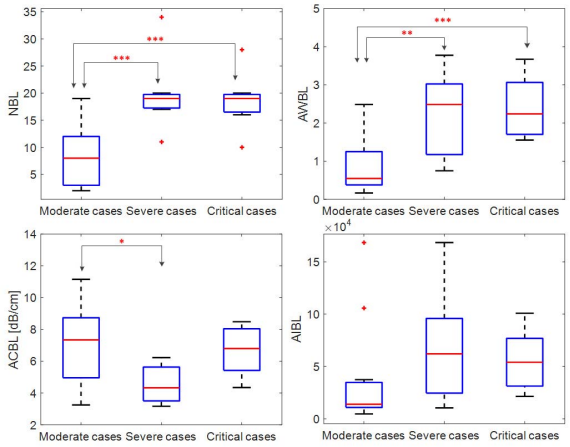

Fig. 5. Comparisons of the BL-related features among moderate cases ($n = 13$), severe cases ($n = 7$), and critical cases ($n = 7$) patients. $^{*}p < 0.05$, $^{**}p < 0.01$, $^{***}p < 0.001$. NBL = number of BLs, AWBL = accumulated width of BLs, ACBL = attenuation coefficient of BLs, and AIBL = accumulated intensity of BLs.

corresponding results of ANOVA with LSD test, respectively. As shown in Fig. 4, for the PL-related features, no significant difference is found between any two groups according to the ANOVA results. Nevertheless, as the disease severity increases, several features, including the TPL, SDPLI, and RPL, show increasing trends, while MPLI shows a decreasing trend. For the BL-related features shown in Fig. 5, significant differences are observed between moderate cases and severe cases for NBL ($p < 0.001$), AWBL ($p < 0.01$), and ACBL ($p < 0.05$). Besides, significant differences between moderate cases and critical cases are found for NBL ($p < 0.001$) and AWBL ($p < 0.001$). No significant differences are found between any two groups for AIBL, as well as between severe cases and critical cases for any of the BL-related features.

Table II shows Spearman's correlation results of the proposed features with severity of COVID-19 pneumonia. For PL-related features, RPL shows significant correlation with disease severity ($p < 0.05, r = 0.39$). For BL-related features,

TABLE II
CORRELATIONS OF THE PROPOSED FEATURES WITH SEVERITY OF COVID-19 PNEUMONIA

Features		r	p value
Pleural line	TPL	0.31	0.12
	RPL	0.39	< 0.05*
	MPLI	-0.31	0.12
	SDPLI	0.21	0.30
B-lines	NBL	0.66	< 0.001***
	AWBL	0.70	< 0.001***
	ACBL	0.19	0.34
	AIBL	0.39	< 0.05*

$^{*}p < 0.05$, $^{**}p < 0.01$, $^{***}p < 0.001$. r: Spearman's correlation coefficient. TPL = thickness of pleural line, RPL = roughness of the pleural line, MPLI = mean value of the pleural line intensity, SDPLI = SD of the pleural line intensity, NBL = number of B-lines, AWBL = accumulated width of B-lines, ACBL = attenuation coefficient of B-lines, AIBL = accumulated intensity of B-lines.

significant correlations with disease severity are found for NBL ($p < 0.001, r = 0.66$), AWBL ($p < 0.001, r = 0.70$), and AIBL ($p < 0.05, r = 0.39$).

C. Binary Classification of Non-Severe and Severe Patients

Table III presents the classification results of each feature, as well as the results of SVM classifiers using features related to PL, BLs, and their combination as input features, respectively. For each method, the AUC under the ROC curve, SEN, and SPC corresponding to the optimal cut-off value on the ROC curve are presented. As shown, among the features related to PL, RPL achieves the best classification performance (AUC = 0.81, SEN = 0.86, SPC = 0.77). The performance is improved using SVM classifier with all PL-related features as input (AUC = 0.87, SEN = 0.86, SPC = 0.93). For BL-related features, NBL and AWBL achieve the same classification performance (AUC = 0.91, SEN = 0.86, SPC = 0.92), and both of them outperform the other two features with larger AUC. Improved classification performance is obtained using SVM classifier with all BL-related features as input (AUC = 0.94, SEN = 0.93, SPC = 0.86). When using all the proposed features as input of SVM classifier, the best classification performance is achieved with largest AUC (0.96), SEN (0.93), and SPC (1.00) among all the compared methods. The ROC curves obtained from SVM classifiers using various combinations of features as input are provided in Fig. 6.

IV. DISCUSSIONS

Specific image patterns in LUS images such as thickening, irregularity, disruption of PL, and confluence of BLs are

TABLE III
CLASSIFICATION RESULTS OF EACH FEATURE AND SVM CLASSIFIERS USING VARIOUS COMBINATIONS OF FEATURES AS INPUT FEATURES

Features		SEN	SPC	AUC [95% CI]
Pleural line	TPL	0.71	0.69	0.68 [0.47-0.88]
	RPL	**0.86**	**0.77**	**0.81 [0.64-0.99]**
	MPLI	0.43	0.92	0.69 [0.49-0.89]
	SDPLI	0.86	0.54	0.65 [0.43-0.88]
	SVM	0.86	0.93	0.87 [0.72-1.00]
B-lines	**NBL**	**0.86**	**0.92**	**0.91 [0.80-1.00]**
	AWBL	**0.86**	**0.92**	**0.91 [0.80-1.00]**
	ACBL	0.93	0.46	0.70 [0.49-0.90]
	AIBL	0.93	0.62	0.74 [0.54-0.94]
	SVM	0.93	0.86	0.94 [0.86-1.00]
SVM (PL+BL)		0.93	1.00	0.96 [0.88-1.00]

TPL = thickness of pleural line, RPL = roughness of the pleural line, MPLI = mean value of the pleural line intensity, SDPLI = SD of the pleural line intensity, NBL = number of B-lines, AWBL = accumulated width of B-lines, ACBL = attenuation coefficient of B-lines, AIBL = accumulated intensity of B-lines. SVM = support vector machine, PL = pleural line, BL = B-lines. SEN = sensitivity, SPC = specificity, AUC = area under the receiver operating characteristics curve, CI = confidence level.

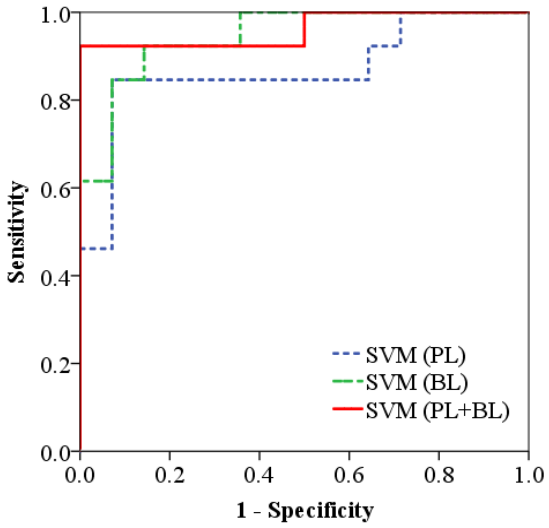

Fig. 6. ROC curves obtained from SVM classifiers using features related to PL, BL, and their combination (PL + BL) as input features, respectively.

found to be associated with the aggravation of COVID-19 pneumonia [8], [22]. However, LUS-based assessment of lung conditions and disease severity depends on the qualitative and subjective observations of clinicians. Therefore, in this study, features related to PL and BLs are extracted from LUS images to quantitatively characterize the image patterns in patients with COVID-19 pneumonia. The performances of these features in assessing the disease severity and classifying non-severe and severe patients are evaluated.

In previous studies, various semiquantitative methods, i.e., scoring systems, based on LUS image patterns were proposed to evaluate the severity of COVID-19 pneumonia and achieved high consistency with chest CT [32], [43]–[45]. However, such scoring systems still rely on the experiences of clinicians. Quantitative methods based on automatic detection of PL [20] or BLs [32] have also been proposed to aid the diagnosis of COVID-19 pneumonia. But these studies mainly focused on intensity-related properties of PL or distribution of BLs and did not consider PL- and BL-related characteristics simultaneously. Some deep-learning-based techniques have shown promises in automatic detection of B lines and pleural effusion, binary classification, and four-level scoring system using artificially extracted quantitative parameters, frame-level and video-level ultrasound images or combination of images, and clinical information as input [33], [34], [36], [46], [47], but they need a large number of annotated samples and have poor interpretability. As a contrast, the quantitative method we

propose aims at characterizing the image patterns of clinical findings and digging out more features from PL and BLs, which are further combined to provide more comprehensive information for severity assessment.

In this study, the classification standard of patients is designed according to the Chinese diagnosis and treatment protocol for novel coronavirus pneumonia (seventh edition) released by the National Health Commission of China and National Administration of Traditional Chinese Medicine, instead of the image scores based on visual judgments of ultrasound images or CT images. Compared with the imaging score-based methods, the classification standard based on comprehensive clinical manifestations (including CT images) according to the clinical diagnosis and treatment protocol provides an overall condition of the patient, which might have highlighted reference value for clinical diagnosis and treatment.

For analysis of PL, four features are extracted, namely, TPL, RPL, MPLI, and SDPLI. TPL is defined with a 75% threshold after parameter optimization, which provides the boundaries of PL closest to those determined by clinicians through visual inspection. A larger TPL indicates the thickening of PL. A larger RPL means a larger variance of depth profile obtained from the center of PL, which may be an indicator of irregularity and disruption of PL. When the lung is in pathological state, the porosity in the sub-pleural tissue may be changed, and thus acoustic impedance difference between the chest wall and the pulmonary containing air may be subsequently changed, which will ultimately affect the PL intensity. For patients with COVID-19 pneumonia, the PL intensity is hypothesized to decrease as the degree of disease severity increases because of pulmonary effusion, consolidation, and confluent BLs, while the SD of the pleural intensity increases because of irregularity and disruption of PL [20]. As shown in Fig. 4 and Table II, increasing trends of TPL, RPL, and SDPLI are observed as the disease becomes severer, and a decreasing trend of the MPLI is observed in contrast. These trends are consistent with the expectations, but the correlations between features and disease severity, and the differences between any two cases are not statistically significant.

For the analysis of BLs, four features are extracted, namely, NBL, AWBL, ACBL, and AIBL. A larger NBL and AWBL (normalized by the length of PL) are hypothesized to be indicators of the confluence of BLs, even in a white lung [39], [48], [49]. BL width is defined with a 75% threshold after parameter optimization, which provides the closest width to that determined by clinicians through visual inspection. Under ill condition of the lung, the porosity in the sub-pleural tissue may be changed due to diffuse alveolar damage or pulmonary inflammation and is characterized by irregular and hyperechoic BLs [50]. ACBL is thus extracted to characterize the attenuation degree of BLs. AIBL may be changed as well due to the combined impacts of AWBL and ACBL. As shown in Fig. 5 and Table II, using NBL, the differences between moderate cases and severe cases and between moderate cases and critical cases are statistically significant, which are in accordance with the hypothesis. ACBLs obtained from severe cases are significantly lower than those from moderate cases. However, the difference between moderate cases and critical cases is not statistically significant using this feature. Possible explanations for this finding could be that the complex lung environment in critical cases interferes the calculation of ACBL and the sample size is too small. Significant differences between any two cases are not found in AIBL, but an increase trend of AIBL is observed with the increase in disease severity degree. The difference between severe cases and critical cases is not found in any features. A possible explanation of this observation may be that patients are identified as critical cases because they are older and have severe concomitant diseases, and thus show more obvious clinical symptoms than severe cases. However, the lung conditions of these patients may be similar and difficult to differentiate based on LUS images.

Among PL-related features, RPL achieves the best performance in differentiating between severe and non-severe patients. Its performance is improved using SVM classifier using all the PL-related features as input. Similarly, NBL and AWBL achieve the best distinguishing performance among all the single features, and SVM classifier using all the BL-related features as input achieves improved performance. The SVM classifier using all the proposed features as input achieves the largest AUC and highest SEN and SPC among all the compared methods because the most comprehensive characteristics are used. It should be noted that SPC reaches 100% and this may be due to the small sample size.

The imaging parameters, including imaging depth, overall gain, TGC, and focal depth, were slightly tuned by clinicians to obtain the best possible imaging field of view and image quality for diagnosis. In the pre-processing step, all the images were normalized in terms of pixel intensity and pixel size to minimize the effects of varying overall gains and imaging depths, respectively. However, such processing cannot eliminate the intensity variances among the acquired images introduced by the differences in TGC, focal depth, and thickness of intercostal layers, which is a limitation of this retrospective study and may be responsible for unsatisfying severity assessment and binary classification performances of intensity-related features, such as MPLI, SDPLI, AWBL, and AIBL (Tables II and III). It should be noted that this is a common limitation of most retrospective studies in current literature [20], [32], [36], [54]. Fortunately, ACBL is mainly affected by TGC, which is slightly tuned during examination, and thus the changes in gains as a function of depth among different patients may be small, and significant differences between moderate and severe cases can still be found using ACBL (Fig. 5). It should be noted that although the dynamic range was kept constant in this study, the influence of dynamic range has been minimized in the calculation of ACBL by multiplying normalized attenuation coefficient with dynamic range, making the results with different dynamic ranges comparable. For a well-designed experiment where the imaging parameters are maintained, the variances of image intensities can be minimized, and thus the proposed intensity-related features may achieve improved diagnosis performance.

NBL is counted by an experienced clinician, which is a limitation of this study. In clinical practice, counting the NBL is an important pathological routine for ultrasound diagnosis of lung diseases and its determination is associated with both defining criteria and counting protocol. A typical BL can be easily identified as a hyperechoic reverberation artifact originating from PL, extending to the bottom of the imaging field of view and moving synchronously with pleural sliding. However, there is a lack of criteria about how to quantify BLs in each intercostal space. In [42], three commonly used counting methods are compared, and the method using percentages of rib spaces covered by fused BLs and counting BLs at the instant of highest incidence shows the highest reliability among all the methods, which is thus used in our study as the counting protocol.

Another limitation of this study is that the locations of PL and BLs are semi-automatically detected. In the semi-automatic detection steps, a rough region is manually selected around the PL or BL for determination of their center positions. The delineated region should be large enough to include the entire PL or BL visible in the field of view, which is helpful to ensure consistency between different patients. Many automatic methods for detection of PL and localization of BLs have been proposed based on various image processing algorithms and deep learning networks [20], [32], [33], [35], [48], [51]–[55]. In the future, PL and BLs will be full automatically detected to develop a more intelligent diagnostic system for COVID-19 pneumonia. Other features, such as statistic distribution parameters of BL speckles, will be extracted for quantitative analysis. Besides, lung consolidation is not considered in this study because it only exists in some patients. It is thus challenging to fairly compare the severity of patients with and without lung consolidations using the related indices. For an assessment method based on deep learning, a determination of the absence or presence of lung consolidation or the related quantitative indices may be used to facilitate the diagnosis performance. For each scanned region, only a representative ultrasound image was recorded for quantitative analysis to reflect the severest lung condition of the patient. If the PL or BL is invisible in the recorded image, NBL and AWBL are calculated as zero for this region, and the PL-related parameters, including TPL, RPL, MPLI, and SDPLI, and other BL-related parameters, including the ACBL and AIBL, are calculated as the average values from other image regions. If a video-level ultrasound images can be recorded, a more comprehensive information concerning the entire respiratory cycle may be obtained using the proposed method. In such case, the parameter for each image region can be calculated from the representative image selected from the video, or calculated as the average of the parameters from different images in the video. Moreover, more patients should be enrolled to evaluate the reliability and repeatability of the proposed method.

The presence of multiple diffuse BLs indicates the presence of interstitial syndrome, which can be caused by pulmonary edema of various causes, interstitial pneumonia, pneumonitis, and pulmonary fibrosis [56]–[58]. Therefore, the BL-related parameters proposed in this study, especially NBL and AWBL, can be used for severity assessment and prognostic evaluation of acute and chronic conditions with diffuse interstitial involvement, including COVID-19 pneumonia. In contrast, irregular, thickened, and interrupted PL mainly appear under the condition of pulmonary fibrosis and acute respiratory distress syndrome (ARDS), including COVID-19 pneumonia, and rarely appear under the condition of acute cardiogenic pulmonary edema (ACPE) [58], [59]. Therefore, PL patterns, which can be characterized by PL-related parameters in this study, may be used to effectively differentiate ACPE from ARDS and pulmonary fibrosis.

V. Conclusion

In this study, we analyze the LUS images by extracting various features related to PL and BLs to assess the severity of COVID-19 pneumonia. These features can quantitatively characterize the specific image patterns associated with disease severity. Features such as RPL, NBL, AWBL, and AIBL show significant correlations with disease severity. SVM classifier using all the features as input achieves optimal performance in binary classification of non-severe and severe patients (AUC = 0.96, SEN = 0.93, SPC = 1.00). The proposed method has potential application in automatic grading diagnosis and follow-up of patients with COVID-19 pneumonia.

References

[1] C. Huang, Y. Wang, X. Li, L. Ren, and B. Cao, "Clinical features of patients infected with 2019 novel coronavirus in Wuhan, China," *Lancet*, vol. 395, pp. 497–506, May 2020.

[2] J. P. Kanne, B. P. Little, J. H. Chung, B. M. Elicker, and L. H. Ketai, "Essentials for radiologists on COVID-19: An update—Radiology scientific expert panel," *Radiology*, vol. 296, no. 2, pp. E113–E114, Aug. 2020.

[3] X. Mei *et al.*, "Artificial intelligence-enabled rapid diagnosis of patients with COVID-19," *Nature Med.*, vol. 26, pp. 1–5, Aug. 2020.

[4] M. Mossa-Basha, C. C. Meltzer, D. C. Kim, M. J. Tuite, K. P. Kolli, and B. S. Tan, "Radiology department preparedness for COVID-19: Radiology scientific expert review panel," *Radiology*, vol. 296, no. 2, pp. E106–E112, Aug. 2020.

[5] M. Chung *et al.*, "CT imaging features of 2019 novel coronavirus (2019-nCoV)," *Radiology*, vol. 295, no. 1, pp. 202–207, 2020.

[6] N. Lessmann, C. I. Sánchez, L. Beenen, L. H. Boulogne, and B. V. Ginneken, "Automated assessment of CO-RADS and chest CT severity scores in patients with suspected COVID-19 using artificial intelligence," *Radiology*, vol. 298, pp. E18–E28, Jul. 2020.

[7] H. X. Bai, R. Wang, Z. Xiong, B. Hsieh, and W. H. Liao, "AI augmentation of radiologist performance in distinguishing COVID-19 from pneumonia of other etiology on chest CT," *Radiology*, vol. 296, pp. E156–E165, Apr. 2020.

[8] S. Manna *et al.*, "COVID-19: A multimodality review of radiologic techniques, clinical utility, and imaging features," *Radiol., Cardiothoracic Imag.*, vol. 2, no. 3, Jun. 2020, Art. no. e200210.

[9] E. Poggiali *et al.*, "Can lung US help critical care clinicians in the early diagnosis of novel coronavirus (COVID-19) pneumonia?" *Radiology*, vol. 295, no. 3, p. E6, Jun. 2020.

[10] D. Buonsenso, A. Piano, F. Raffaelli, N. Bonadia, and F. Franceschi, "Point-of-care lung ultrasound findings in novel coronavirus disease-19 pnemoniae: A case report and potential applications during COVID-19 outbreak," *European Rev. Med. Pharmacol. Sci.*, vol. 24, pp. 2776–2780, Apr. 2020.

[11] Q.-Y. Peng, X.-T. Wang, and L.-N. Zhang, "Findings of lung ultrasonography of novel corona virus pneumonia during the 2019–2020 epidemic," *Intensive Care Med.*, vol. 46, no. 5, pp. 849–850, May 2020.

[12] A. Hussain *et al.*, "Multi-organ point-of-care ultrasound for COVID-19 (PoCUS4COVID): International expert consensus," *Crit. Care*, vol. 24, no. 1, p. 702, Dec. 2020.

[13] F. Qian, X. Zhou, J. Zhou, Z. Liu, and Q. Nie, "A valuable and affordable handheld ultrasound in combating COVID-19," *Crit. Care*, vol. 24, no. 1, p. 334, Dec. 2020.

[14] J. Sun, Q. Li, X. Wu, X. Wang, and D. Liu, "Nurse-performed ultrasound: A new weapon against COVID-19," *Crit. Care*, vol. 24, no. 1, p. 430, Dec. 2020.

[15] F. Roy-Gash, M. De Mesmay, J.-M. Devys, H. Vespignani, R. Blanc, and N. Engrand, "COVID-19-associated acute cerebral venous thrombosis: Clinical, CT, MRI and EEG features," *Crit. Care*, vol. 24, no. 1, p. 419, Dec. 2020.

[16] G. Soldati, M. Demi, A. Smargiassi, R. Inchingolo, and L. Demi, "The role of ultrasound lung artifacts in the diagnosis of respiratory diseases," *Expert Rev. Respiratory Med.*, vol. 13, no. 2, pp. 163–172, Feb. 2019.

[17] P. Enghard *et al.*, "Simplified lung ultrasound protocol shows excellent prediction of extravascular lung water in ventilated intensive care patients," *Crit. Care*, vol. 19, no. 1, p. 36, 2015.

[18] G. Baldi *et al.*, "Lung water assessment by lung ultrasonography in intensive care: A pilot study," *Intensive Care Med.*, vol. 39, no. 1, pp. 74–84, Jan. 2013.

[19] G. Soldati, M. Demi, R. Inchingolo, A. Smargiassi, and L. Demi, "On the physical basis of pulmonary sonographic interstitial syndrome," *J. Ultrasound Med.*, vol. 35, no. 10, pp. 2075–2086, Oct. 2016.

[20] L. Carrer *et al.*, "Automatic pleural line extraction and COVID-19 scoring from lung ultrasound data," *IEEE Trans. Ultrason., Ferroelectr., Freq. Control*, vol. 67, no. 11, pp. 2207–2217, Nov. 2020.

[21] M. Sperandeo, C. M. I. Quarato, and G. Rea, "Diagnosis of coronavirus disease 2019 pneumonia in pregnant women: Can we rely on lung ultrasound?" *Amer. J. Obstetrics Gynecol.*, vol. 223, no. 4, p. 615, Oct. 2020.

[22] C. Xing, Q. Li, H. Du, W. Kang, J. Lian, and L. Yuan, "Lung ultrasound findings in patients with COVID-19 pneumonia," *Crit. Care*, vol. 24, no. 1, p. 174, Dec. 2020.

[23] D. Buonsenso *et al.*, "Clinical role of lung ultrasound for diagnosis and monitoring of COVID-19 pneumonia in pregnant women," *Ultrasound Obstetrics Gynecol.*, vol. 56, no. 1, pp. 106–109, Jul. 2020.

[24] P. Lomoro *et al.*, "COVID-19 pneumonia manifestations at the admission on chest ultrasound, radiographs, and CT: Single-center study and comprehensive radiologic literature review," *Eur. J. Radiol. Open*, vol. 7, Jan. 2020, Art. no. 100231.

[25] S. Sofia *et al.*, "Thoracic ultrasound and SARS-COVID-19: A pictorial essay," *J. Ultrasound*, vol. 23, no. 2, pp. 217–221, Jun. 2020.

[26] G. Soldati *et al.*, "Proposal for international standardization of the use of lung ultrasound for patients with COVID-19," *J. Ultrasound Med.*, vol. 39, pp. 1413–1419, Jul. 2020.

[27] M. J. Smith, S. A. Hayward, S. M. Innes, and A. S. C. Miller, "Point-of-care lung ultrasound in patients with COVID-19—A narrative review," *Anaesthesia*, vol. 75, pp. 1096–1104, Aug. 2020.

[28] L. Vetrugno *et al.*, "Our Italian experience using lung ultrasound for identification, grading and serial follow-up of severity of lung involvement for management of patients with COVID-19," *Echocardiography*, vol. 37, no. 4, pp. 625–627, 2020.

[29] G. Volpicelli and L. Gargani, "Sonographic signs and patterns of COVID-19 pneumonia," *Ultrasound J.*, vol. 12, no. 1, p. 22, Dec. 2020.

[30] W. Lu *et al.*, "A clinical study of noninvasive assessment of lung lesions in patients with coronavirus disease-19 (COVID-19) by bedside ultrasound," *Ultraschall Medizin Eur. J. Ultrasound*, vol. 41, no. 3, pp. 300–307, Jun. 2020.

[31] M. Allinovi *et al.*, "Lung ultrasound may support diagnosis and monitoring of COVID-19 pneumonia," *Ultrasound Med. Biol.*, vol. 46, no. 11, pp. 2908–2917, Nov. 2020.

[32] Q. Deng *et al.*, "Semiquantitative lung ultrasound scores in the evaluation and follow-up of critically ill patients with COVID-19: A single-center study," *Academic Radiol.*, vol. 27, no. 10, pp. 1363–1372, Oct. 2020.

[33] J. Chen *et al.*, "Quantitative analysis and automated lung ultrasound scoring for evaluating COVID-19 pneumonia with neural networks," *IEEE Trans. Ultrason., Ferroelectr., Freq. Control*, vol. 68, no. 7, pp. 2507–2515, Jul. 2021.

[34] S. Roy *et al.*, "Deep learning for classification and localization of COVID-19 markers in point-of-care lung ultrasound," *IEEE Trans. Med. Imag.*, vol. 39, no. 8, pp. 2676–2687, Aug. 2020.

[35] R. J. G. van Sloun and L. Demi, "Localizing B-lines in lung ultrasonography by weakly supervised deep learning, *in-vivo* results," *IEEE J. Biomed. Health Informat.*, vol. 24, no. 4, pp. 957–964, Apr. 2020.

[36] W. Xue *et al.*, "Modality alignment contrastive learning for severity assessment of COVID-19 from lung ultrasound and clinical information," *Med. Image Anal.*, vol. 69, Apr. 2021, Art. no. 101975.

[37] N. Awasthi, A. Dayal, L. R. Cenkeramaddi, and P. K. Yalavarthy, "Mini-COVIDNet: Efficient lightweight deep neural network for ultrasound based point-of-care detection of COVID-19," *IEEE Trans. Ultrason., Ferroelectr., Freq. Control*, vol. 68, no. 6, pp. 2023–2037, Jun. 2021.

[38] P. F. Wei, "Diagnosis and treatment protocol for novel coronavirus pneumonia (trial version 7)," *Chin. Med. J.*, vol. 133, no. 9, pp. 1087–1095, 2020, doi: 10.1097/CM9.0000000000000819).

[39] A. Soummer *et al.*, "Ultrasound assessment of lung aeration loss during a successful weaning trial predicts postextubation distress," *Crit. Care Med.*, vol. 40, pp. 2064–2072, Jul. 2012.

[40] F. P. Caltabeloti *et al.*, "Early fluid loading in acute respiratory distress syndrome with septic shock deteriorates lung aeration without impairing arterial oxygenation: A lung ultrasound observational study," *Crit. Care*, vol. 18, no. 3, pp. 1–11, Jun. 2014.

[41] B. Bouhemad, M. Zhang, Q. Lu, and J.-J. Rouby, "Clinical review: Bedside lung ultrasound in critical care practice," *Crit. Care*, vol. 11, no. 1, p. 205, Feb. 2007.

[42] K. L. Anderson, J. M. Fields, N. L. Panebianco, K. Y. Jenq, J. Marin, and A. J. Dean, "Inter-rater reliability of quantifying pleural B-lines using multiple counting methods," *J. Ultrasound Med.*, vol. 32, no. 1, pp. 115–120, Jan. 2013.

[43] L. Ji *et al.*, "Prognostic value of bedside lung ultrasound score in patients with COVID-19," *Crit. Care*, vol. 24, no. 1, p. 700, Dec. 2020.

[44] L. Zhao *et al.*, "Lung ultrasound score in evaluating the severity of coronavirus disease 2019 (COVID-19) pneumonia," *Ultrasound Med. Biol.*, vol. 46, no. 11, pp. 2938–2944, Nov. 2020.

[45] F. Zhu *et al.*, "Ultrasonic characteristics and severity assessment of lung ultrasound in COVID-19 pneumonia in Wuhan, China: A retrospective, observational study," *Engineering*, vol. 7, no. 3, pp. 367–375, Mar. 2021, doi: 10.1016/j.eng.2020.09.007.

[46] A. G. Dastider, F. Sadik, and S. A. Fattah, "An integrated autoencoder-based hybrid CNN-LSTM model for COVID-19 severity prediction from lung ultrasound," *Comput. Biol. Med.*, vol. 132, May 2021, Art. no. 104296.

[47] C.-H. Tsai *et al.*, "Automatic deep learning-based pleural effusion classification in lung ultrasound images for respiratory pathology diagnosis," *Phys. Medica*, vol. 83, pp. 38–45, Mar. 2021.

[48] C. Brusasco *et al.*, "Quantitative lung ultrasonography: A putative new algorithm for automatic detection and quantification of B-lines," *Crit. Care*, vol. 23, no. 1, p. 288, Dec. 2019.

[49] S. Mongodi *et al.*, "Modified lung ultrasound score for assessing and monitoring pulmonary aeration," *Ultraschall Medizin Eur. J. Ultrasound*, vol. 38, no. 5, pp. 530–537, Oct. 2017.

[50] G. Soldati, A. Smargiassi, L. Demi, and R. Inchingolo, "Artifactual lung ultrasonography: It is a matter of traps, order, and disorder," *Appl. Sci.*, vol. 10, no. 5, p. 1570, Feb. 2020.

[51] K. L. Hansen *et al.*, "Novel automatic detection of pleura and B-lines (comet-tail artifacts) on *in vivo* lung ultrasound scans," *Proc. SPIE.*, vol. 9790, Apr. 2016, Art. no. 97900K.

[52] R. Moshavegh, K. L. Hansen, H. Møller-Sørensen, M. B. Nielsen, and J. A. Jensen, "Automatic detection of B-lines in *in vivo* lung ultrasound," *IEEE Trans. Ultrason., Ferroelectr., Freq. Control*, vol. 66, no. 2, pp. 309–317, Dec. 2018.

[53] C. Baloescu *et al.*, "Automated lung ultrasound B-line assessment using a deep learning algorithm," *IEEE Trans. Ultrason., Ferroelectr., Freq. Control*, vol. 67, no. 11, pp. 2312–2320, Nov. 2020.

[54] N. Anantrasirichai, W. Hayes, M. Allinovi, D. Bull, and A. Achim, "Line detection as an inverse problem: Application to lung ultrasound imaging," *IEEE Trans. Med. Imag.*, vol. 36, no. 10, pp. 2045–2056, Oct. 2017.

[55] O. Karakus, N. Anantrasirichai, A. Aguersif, S. Silva, A. Basarab, and A. Achim, "Detection of line artifacts in lung ultrasound images of COVID-19 patients via nonconvex regularization," *IEEE Trans. Ultrason., Ferroelectr., Freq. Control*, vol. 67, no. 11, pp. 2218–2229, Nov. 2020.

[56] G. Volpicelli *et al.*, "International evidence-based recommendations for point-of-care lung ultrasound," *Intensive Care Med.*, vol. 38, pp. 577–591, Apr. 2012.

[57] G. Volpicelli *et al.*, "Bedside lung ultrasound in the assessment of alveolar-interstitial syndrome," *Amer. J. Emergency Med.*, vol. 24, pp. 689–696, Oct. 2006.
[58] P. Mayo *et al.*, "Thoracic ultrasonography: A narrative review," *Intensive care Med.*, vol. 45, pp. 1200–1211, Sep. 2019.
[59] R. Copetti, G. Soldati, and P. Copetti, "Chest sonography: A useful tool to differentiate acute cardiogenic pulmonary edema from acute respiratory distress syndrome," *Cardiovascular Ultrasound*, vol. 6, no. 1, p. 16, 2008.

Yuanyuan Wang (Student Member, IEEE) received the B.S. degree in biomedical engineering from the School of Biomedical Engineering, Capital Medical University, Beijing, China, in 2016. She is currently pursuing the Ph.D. degree with the Department of Biomedical Engineering, Tsinghua University, Beijing.

Her research interests include ultrasound elasticity imaging and ultrasonic tissue characterization based on ultrasound images and radio-frequency signals.

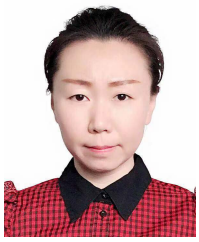

Yao Zhang received the B.S. degree in imaging medicine from the Medical College, Beihua University, Jilin City, Jilin, China, in 2004, and the M.S. degree in imaging medicine and nuclear medicine from Capital Medical University, Beijing, China, in 2018.

She is currently an Associate Chief Physician with the Department of Ultrasound, Beijing Ditan Hospital affiliated to Capital Medical University.

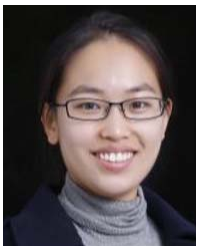

Qiong He (Member, IEEE) received the B.S. degree in biomedical engineering from Capital Medical University, Beijing, China, in 2012, and the Ph.D. degree in biomedical engineering from Tsinghua University, Beijing, in 2017.

She was a Post-Doctoral Research Scientist from 2017 to 2020 and a Research Associate Professor from 2020 to 2021 with the Department of Biomedical Engineering, Tsinghua University. She is currently a Chief Scientist at Wuxi Hisky Medical Technologies Company Ltd., Beijing. She was supported by the Chinese Post-Doctoral Science Foundation in 2017. She received the Young Scientists Fund from the National Natural Science Foundation of China (NSFC) in 2018 and the Young Elite Scientists Sponsorship by China Association for Science and Technology in 2019. Her current research interests include system development and medical imaging.

Hongen Liao (Senior Member, IEEE) received the B.S. degree in mechanics and engineering sciences from Peking University, Beijing, China, in 1996, and the M.E. and Ph.D. degrees in precision machinery engineering from the University of Tokyo, Tokyo, Japan, in 2000 and 2003, respectively.

He was a Research Fellow of the Japan Society for the Promotion of Science. Since 2004, he has been a Faculty Member at the Graduate School of Engineering, University of Tokyo, where he became an Associate Professor in 2007. He has been selected as a National Distinguished Professor, China, since 2010. He is currently a Full Professor and the Vice Dean of the School of Medicine and the Department of Biomedical Engineering, Tsinghua University, Beijing. He is the author and coauthor of more than 300 peer-reviewed articles and proceedings papers, as well as over 50 patents, 320 conference abstracts, and numerous invited lectures. His research interests include 3-D medical imaging, image-guided surgery, medical robotics, computer-assisted surgery, and the fusion of these techniques for minimally invasive precision diagnosis and therapy.

Dr. Liao was distinguished by receiving the government awards and various best paper awards from different academic societies. He is an Associate Editor of IEEE Engineering in Medicine and Biology Society (EMBS) Conference, and he has been the Organization Chair of Medical Imaging and Augmented Reality Conference (MIAR) in 2008, the Program Chair of the Asian Conference on Computer-Aided Surgery Conference (ACCAS) from 2008 to 2009, the Tutorial Co-Chair of the Medical Image Computing and Computer Assisted Intervention Conference (MICCAI) in 2009, the Publicity Chair of MICCAI in 2010, the General Chair of MIAR in 2010 and ACCAS in 2012, the Program Chair of MIAR in 2013, the Workshop Chair of MICCAI in 2013 and MICCAI in 2019, and the General Co-Chair of MIAR in 2016 and ACCAS in 2018. He served as the President for Asian Society for Computer Aided Surgery and the Co-Chair of Asian–Pacific Activities Working Group, International Federation for Medical and Biological Engineering (IFMBE).

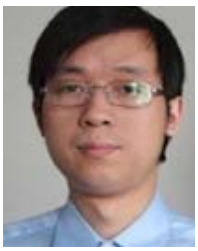

Jianwen Luo (Senior Member, IEEE) received the B.S. and Ph.D. degrees (Hons.) in biomedical engineering from Tsinghua University, Beijing, China, in 2000 and 2005, respectively.

He was a Post-Doctoral Research Scientist from 2005 to 2009 and an Associate Research Scientist from 2009 to 2011 with the Department of Biomedical Engineering, Columbia University, New York City, NY, USA. He joined the Department of Biomedical Engineering and the Center for Biomedical Imaging Research, Tsinghua University, as a Tenure Track Associate Professor in 2011 and became a Tenured Associate Professor in 2017. He was enrolled in the Thousand Young Talents Program of China in 2012, and received the Excellent Young Scientists Fund from the National Natural Science Foundation of China (NSFC) in 2013. He was supported by the National Key R&D Program of China in 2016 and 2020. He has authored or coauthored over 165 peer-reviewed articles in international journals, 90 conference proceedings papers, and 200 conference abstracts. His research interests include ultrasound imaging, fluorescence imaging, and photoacoustic imaging.

Dr. Luo serves as a member of the IEEE Engineering in Medicine and Biology Society (EMBS) Technical Committee on Biomedical Imaging and Image Processing (BIIP) and the Technical Program Committee of IEEE International Ultrasonics Symposium (IUS). He serves as an Associate Editor for IEEE TRANSACTIONS ON ULTRASONICS, FERROELECTRICS, AND FREQUENCY CONTROL and an Advisory Editorial Board Member of *Journal of Ultrasound in Medicine*.